ROYAL SOCIETY
OF CHEMISTRY

Check for updates

Atomically dispersed Pt catalyst on ceria-carbon for suppressing C−C cleavage in glycerol electrooxidation

Hae Ryeong Lee,[†a] Eunchong Lee,[†b] Yunji Choi,[a] Jaehoon Kwon, [ID][a] Seonmin Jeon,[a] Sujin Park,[a] Yun Jeong Hwang [ID] [*b] and Hyunjoo Lee [ID] [*a]

Glycerol, a low-cost and abundant byproduct of biodiesel production, has attracted attention as a feedstock for conversion into value-added chemicals. To maximize the economic value of products, maintaining three carbons (C_3) as the dominant product is important yet difficult to achieve at high potentials due to the favorable C−C bond scission. We demonstrate that an atomically dispersed Pt catalyst anchored on defect-rich ceria-carbon selectively controls the glycerol electrooxidation reaction (GEOR), favoring C_3 products. The isolated Pt sites favored single-carbon adsorption, preventing multi-carbon binding and subsequent cleavage up until high potential of 1.2 V_{RHE}. The catalyst maintained nearly 70% of C_3 selectivity across various potentials with high glycerate productivity and selectivity. In contrast, catalysts with Pt nanoparticles rapidly shifted towards C_2 and C_1 products, especially glycolate and formate as potential increases. Moreover, Pt single atoms on the catalyst maintained high glycerate productivity without much Pt agglomeration under 48 h operation. Beyond batch operation, the Pt single atom catalyst was validated in a continuous flow-cell reactor. Glycerate remained as the major product, reaching a selectivity of 51.6% as potential increases and exhibited a productivity of 37.0 mmol L^{-1} mg_{Pt}^{-1} h^{-1} at 1.2 V_{RHE}. This work highlights atomic dispersion on defect-engineered supports as a powerful strategy to control electrocatalytic pathways in the GEOR *via* suppressing C−C cleavage.

1. Introduction

In recent decades, the search for alternative energy sources has intensified, driven by the urgent need for clean and sustainable solutions. Alongside renewable power sources such as wind, solar, and tidal energy, attention has also focused on energy carriers, specifically biofuels. For instance, the International Energy Agency (IEA) reported that there would be a near 30% increase in biofuel demand over 2023–2028.[1] Among biofuels, biodiesel has become especially prominent due to its abundant sources.[2] The most commonly used method for biodiesel production is transesterification and this process inevitably generates about 10 wt% glycerol as a by-product.[3] As biodiesel production has expanded rapidly, glycerol has become an abundant co-product, causing persistent oversupply. The glycerol supply is expected to increase faster than its conventional market growth (*e.g.*, food and cosmetics).[4,5] In fact, the current estimates suggest that glycerol production is approximately six times greater than the market demand.[6] The oversupply of

glycerol has significantly reduced its market value, leading the U.S. Department of Energy to designate it as a key biomass-derived platform chemical for the synthesis of oxygenated organic compounds.[7,8] As a result, developing efficient strategies to convert glycerol into higher-value chemicals has emerged as a particularly promising approach.

Glycerol electrooxidation (GEOR) using catalysts has emerged as a promising pathway for glycerol valorization.[9–11] The conventional heterogeneous catalytic processes require harsh reaction environments involving pressurization and toxic oxidants such as permanganate and nitric acid.[12,13] However, the GEOR can be carried out efficiently at room temperature, minimizing the operating cost.[14] The primary challenge in the GEOR is the large number of possible reaction pathways, leading to a wide distribution of intermediates and products, including C_3 products (glycerate, tartronate, and lactate), C_2 products (glycolate, acetate) and C_1 products (formate, CO_2).[15–17] Therefore, the catalyst must be carefully chosen to control product selectivity.

Among various products, achieving high selectivity toward C_3 products such as glycerate is important. These molecules preserve the three-carbon backbone of glycerol and possess substantially higher economic value, serving as precursors to fine chemicals, biodegradable polymers, and pharmaceuticals.[18,19] Noble metal catalysts, particularly Pt-based materials,

aDepartment of Chemical and Biomolecular Engineering, Korea Advanced Institute of Science and Technology, Daejon 34141, Republic of Korea. E-mail: azhyun@kaist.ac.kr
bDepartment of Chemistry, College of Natural Sciences, Seoul National University, Seoul 08826, Republic of Korea. E-mail: yjhwang1@snu.ac.kr
† These authors contributed equally.

This journal is © The Royal Society of Chemistry 2026

J. Mater. Chem. A, 2026, **14**, 15075–15084 | 15075

exhibit high intrinsic activity toward glycerol electrooxidation.[20] Yet, its selectivity depends on various factors, such as catalyst composition,[10,12,19] morphology,[21,22] and reaction conditions, such as applied potentials[23] and temperature.[24] To enhance the C_3 selectivity even at high potentials, bimetallic Pt alloys are commonly used. Li *et al.* reported that alloying Pt with Au optimizes the adsorption of the glycerol molecule for one terminal C atom to be adsorbed at the surface, ensuring high C_3 selectivity.[10] Zhou *et al.* reported that alloying Pt with Ru facilitates the formation of C_3 products while alloying Pt with Rh enhances the formation of C_2 products.[12] Because the electrooxidation would occur more at high potentials, the C–C bond should be preserved to ensure high C_3 productivity even at high potentials.[15]

In this work, an atomically dispersed Pt catalyst was prepared on defect-rich ceria, which was anchored on a carbon support, to sustain high C_3 selectivity. Their activity and selectivity for glycerol electrooxidation were compared with those of Pt nanoparticles deposited on the same defect-rich ceria/C support, Pt clusters immobilized on non-defect-rich ceria/C, and commercial Pt/C catalysts. Pt single atoms provided an ideal active site, which allowed glycerol adsorption for electrooxidation but prohibited C–C bond cleavage. This catalyst with Pt single atoms especially promoted glycerate formation with good C_3 selectivity even at a high potential of 1.2 V_{RHE}. Pt nanoparticles promoted C–C bond cleavage, forming more C_2 or C_1 compounds. The stability of Pt single atoms was tested for 48 h and compared with that of the commercial Pt/C. Notably, the same trend for Pt single atoms was reproduced in a continuous flow-cell configuration, which resembles process-relevant operation more closely and might simplify downstream separation.

2. Experimental

2.1. Materials and chemicals

Chloroplatinic acid hexahydrate ($H_2PtCl_6 \cdot 6H_2O$, ≥37.50% Pt basis), ethanol (C_2H_6O, anhydrous, ≤0.005% water), Nafion perfluorinated resin solution (5 wt% in lower aliphatic alcohols/water), phenol (C_6H_5OH, ≥99%), and dimethyl sulfoxide (($CH_3)_2SO$, ≥99.5% (GC), DMSO) were purchased from Sigma-Aldrich. Cerium nitrate ($Ce(NO_3)_3 \cdot 6H_2O$, 99.99%) was purchased from Kanto chemical. 2-Propanol (($CH_3)_2CHOH$, 99.7%) was purchased from Junsei. Hydrogen peroxide (H_2O_2, 34.5%) and potassium hydroxide solution (KOH, 1.0 M) were purchased from Samchun Chemical. Toray 090 carbon paper and Vulcan carbon (XC72) were purchased from the Fuel Cell store.

2.2. Catalyst synthesis

The Vulcan carbon was treated with 6 M H_2O_2 overnight. Then, it was washed, filtered with deionized water, and dried in an oven at 80 °C. Then, 30 wt% ceria was deposited on the treated carbon. An appropriate amount of $Ce(NO_3)_3 \cdot 6H_2O$ was dissolved in ethanol to prepare a cerium precursor solution. After the treated carbon was dispersed in ethanol, the cerium

precursor solution was added and then dried at 85 °C with stirring. The obtained powder was further dried in an oven at 80 °C and heat-treated at 250 °C under N_2 flow for 4 h (Ce-C). Ce-C was reduced at 400 °C for 2 h under 10% H_2 (N_2 balance) to produce CeR-C. Lastly, either 0.3 or 1 wt% of Pt was impregnated on the CeR-C support. The Pt precursor solution was prepared by dissolving an appropriate amount of $H_2PtCl_6 \cdot 6H_2O$ in ethanol. The support (CeR-C or Ce-C) was dispersed in ethanol, and the Pt precursor solution was subsequently added dropwise under stirring and dried at 85 °C. After reducing the final powder at 250 °C for 1 h under 10% H_2 (N_2 balance), the catalyst was prepared for evaluation. For comparison, 1 wt% Pt nanoparticles, which were synthesized by a polyol method using ethylene glycol, were deposited on CeR-C (1Pt NP-CeR-C).[25]

2.3. Characterization

High-angle annular dark field-scanning transmission electron microscopy (HAADF-STEM) was carried out using a Titan cubed G2 60-300 (FEI), operating at an accelerating voltage of 300 kV. X-ray photoelectron spectroscopy (XPS) was performed using K-alpha (ThermoVG Scientific) to analyze the electronic properties of Ce. Binding energies were calculated with respect to C 1s at 284.8 eV. H_2-temperature programmed reduction (H_2-TPR) was achieved using a BELCAT-B (BELCAT). Ce-C was pretreated with either Ar at 100 °C for 30 min, or with 5% H_2 (Ar balance) at 400 °C for 2 h to mimic CeR-C. H_2-TPR was performed by increasing the temperature to 900 °C with a rate of 10 °C min^{-1}. X-ray diffraction (XRD) was conducted on a SmartLab (Rigaku) using Cu Kα radiation. The extended X-ray absorption fine structure (EXAFS) was obtained using 8C Nano XAFS and 10C Wide XAFS beamlines at the Pohang Accelerator Laboratory (PAL). The data was processed and simulated using ATHENA and ARTEMIS.

2.4. Electrochemical measurements

All the electrochemical measurements were performed at room temperature using a potentiostat (CHI730E). A Hg/HgO electrode and a carbon rod were used as a reference and a counter electrode, respectively. Before and during the measurements, N_2 gas was continuously purged to remove oxygen in the electrolytes. The measured potentials were converted to the reversible hydrogen electrode (RHE) scale and reported in this work using the following equation:

$$E_{RHE} = E_{Hg/HgO} + 0.059 \times pH + 0.098$$

Catalysts were loaded on the carbon paper using a spraying gun and a batch type three-electrode system was used for the electrochemical measurements. A catalyst ink was prepared by sonicating the mixture of catalyst (9 mg), deionized water (0.7 ml), isopropyl alcohol (2.1 ml), and 5 wt% Nafion ionomer solution (128 μl). The catalyst ink was sprayed on carbon paper with a loading of 0.05 mg_{Pt} cm^{-2} and an electrode area of 1 cm^2. Before every measurement, 50 cycles of voltage sweep were conducted using a cyclic voltammetry (CV) method in the

15076 | *J. Mater. Chem. A*, 2026, **14**, 15075–15084

This journal is © The Royal Society of Chemistry 2026

potential range of 0.05 V_{RHE} to 1.1 V_{RHE} in 1 M KOH with a scan rate of 100 mV s^{-1}. For the methanol oxidation reaction (MOR), an electrolyte of 1 M KOH with 0.5 M methanol was used. It was conducted *via* the CV method in the same potential range with activation but with a scan rate of 10 mV s^{-1}. The electrolyte was changed to 1 M KOH with 0.1 M glycerol for GEOR measurement. The chronoamperometry (CA) technique was applied at various potentials (0.6, 0.8, 1.0 and 1.2 V_{RHE}) for 3 h to evaluate the catalysts' performance. For the stability test, the CA technique was applied for 48 h at 1.0 V_{RHE}.

To further assess the practical performance of the catalyst, flow cell measurements were conducted. The catalyst ink was sprayed on carbon paper with a loading of 0.05 mg$_{Pt}$ cm^{-2} for the anode and 0.1 mg$_{Pt}$ cm^{-2} for the cathode. The synthesized catalyst and commercial 20% Pt/C were used as the anode and cathode, respectively. A Mini-hydroflex was used as a reference electrode. Either 1 M KOH with 0.1 M or 0.5 M glycerol was circulated at the anode while 1 M KOH was circulated at the cathode, with a flow rate of 10 or 20 sccm. Both electrolytes were purged with N$_2$ gas during the measurement. The CA technique was applied at various potentials for 3 h to evaluate the catalyst performance. The detailed illustrations of the batch system and flow cell are shown in Fig. S1 and S2.

2.5. Product quantification

The GEOR products were collected and examined using an online gas chromatography (GC; Micro GC Fusion, Inficon) system equipped with an Rt-Molecular sieve with a 5 Å column and ^{1}H NMR (Avance Neo 400, Bruker) during and after the CA method, respectively. For gas product quantification, the gas outlet from the GEOR reactor was connected to the GC and GC injections were performed every 5 min. The total productivity of gas products was quantified by integrating a plot of concentration *vs.* time. For liquid products, the electrolyte after reaction was detected using an NMR spectrometer. A 640 μl sample after the reaction was collected and mixed with 75 μl of D$_2$O. Phenol and DMSO were added as an internal standard. The selectivity of products was estimated using the following equations:

$$\text{Selectivity (\%)} = \frac{\text{product productivity}}{\text{sum of each product productivities}} \times 100\%$$

2.6. *In situ* Raman spectroscopy analysis

In situ Raman spectroscopy was performed using a custom-built electrochemical cell coupled with a Raman spectrometer (InVia™ Qontor confocal Raman microscope, Renishaw). A 532 nm laser was employed with an exposure time of 10 s, 20 accumulations, and a laser power set to 1%. The as-prepared catalysts deposited on carbon paper were used as the working electrode, while a Hg/HgO (1 M KOH) electrode and a Pt wire served as the reference and counter electrodes, respectively, in 1 M KOH electrolyte with 0.5 M glycerol. Raman spectra under steady-state conditions were obtained by multi-step chronoamperometry (CA) from 0.5 to 1.2 V_{RHE}. To observe M–OH

peaks, the Raman spectra were captured using a 633 nm laser with an exposure time of 60 s, and 3 accumulations.

3. Results and discussion

3.1. Structural characterization of catalysts

The carbon support was treated with H$_2$O$_2$ to provide surface functional groups. Ceria was then deposited through wetness impregnation followed by thermal treatment, producing a Ce-C support. To enrich surface defects for enabling Pt single atom deposition, this support was further reduced under a H$_2$ atmosphere, yielding a CeR-C support. Subsequently, 0.3 wt% or 1 wt% Pt was loaded on these supports, yielding 0.3Pt-CeR-C or 1Pt-CeR-C, respectively (Fig. 1a). HAADF-STEM showed that no Pt cluster was found in both 0.3Pt-CeR-C and 1Pt-CeR-C catalysts and only Pt single atoms, highlighted with yellow circles, were deposited on ceria (Fig. 1b and c and S3). By contrast, increasing the Pt loading to 1.5 and 2 wt% on CeR-C resulted in predominant Pt clusters (Fig. S4), indicating that 1 wt% is the practical upper limit for stabilizing Pt primarily as single atoms. Pt nanoparticles (2.17 ± 0.24 nm), which were separately synthesized *via* the polyol method with ethylene glycol, were deposited on the CeR-C support with 1 wt% Pt (1Pt NP-CeR-C) for comparison (Fig. 1d and S5a). When ceria was not reduced, however, both single atoms and clusters (0.86 ± 0.17 nm) were observed in the 1 wt% Pt sample (1Pt-Ce-C; Fig. 1e and S5b). The formation of defect-rich ceria was essential to immobilize Pt single atoms.

Defects in ceria would lead to oxygen vacancies and they provided sites for Pt single atoms to be strongly anchored on.[26–28] Compared to Ce-C, CeR-C had a much higher number of defects. XPS results clearly showed that after reduction of ceria, the percentage of Ce^{3+} increased significantly from 29.2 to 38.8% (Fig. S6). Even after Pt impregnation, the percentage difference was maintained. H$_2$-TPR was additionally conducted to further clarify defect type and abundance (Fig. S7). Two main reduction features were observed at ~500 °C and ~715 °C, which are assigned to surface oxygen species and bulk/lattice oxygen, respectively.[29] The dominant difference between CeR-C and Ce-C appeared in the surface-related peak, whereas the bulk-related peak showed no change, indicating that the support distinction was mainly associated with surface defects. The integrated H$_2$ consumption in the surface-reduction region was 0.0330 mmol g^{-1} for CeR-C *versus* 0.0533 mmol g^{-1} for Ce-C, suggesting that CeR-C was more pre-reduced at the surface. Both XPS and TPR results support that the higher extent of surface defect sites in CeR-C was the primary contributor to Pt single atom stabilization on ceria-carbon and prevented Pt from being deposited as clusters.

The EXAFS results confirmed that Pt was atomically dispersed on 1Pt-CeR-C and 0.3Pt-CeR-C (Fig. 1f). The presence of the Pt–Cl peak (at 1.9 Å) without the Pt–Pt metallic peak (at 2.6 Å) showed that there were little clusters on those catalysts.[30,31] 1Pt NP/CeR-C clearly showed a large Pt–Pt peak, similar to that of Pt foil. In the case of 1Pt-Ce-C, the dominant peak was the Pt–Cl bond, but the Pt–Pt bond was still noticeable. From the fitting results of EXAFS data (Table S1), the
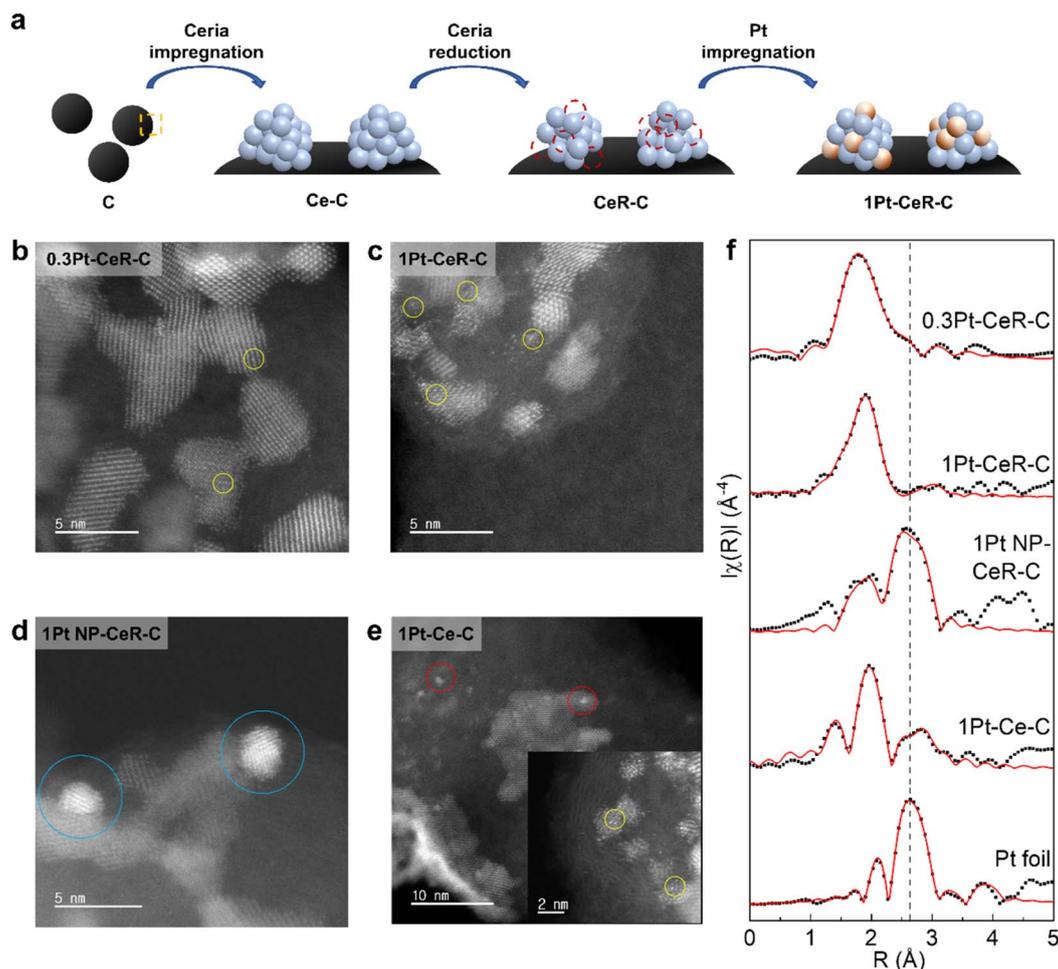
This journal is © The Royal Society of Chemistry 2026

J. Mater. Chem. A, 2026, **14**, 15075–15084 | **15077**

Fig. 1 (a) Schematic illustration of the synthesis procedure for 1Pt–CeR–C. HAADF-STEM images of (b) 0.3Pt–CeR–C, (c) 1Pt–CeR–C, (d) 1Pt NP-CeR–C, and (e) 1Pt–Ce–C. Yellow, red, and blue circles represent Pt single atoms, Pt clusters, and Pt nanoparticles, respectively. (f) Fourier transform of k3-weighted EXAFS data of various Pt catalysts and the Pt foil reference.

coordination numbers (CN) for Pt–Pt in 0.3Pt–CeR–C and 1Pt–CeR–C were 0.6 and 0.8, respectively, confirming their single atom feature. However, the CN for Pt–Pt in 1Pt NP-CeR–C was 8.9. Meanwhile, the CN for Pt–Pt in 1Pt–Ce–C was 1.4 which was significantly higher than that of 0.3Pt–CeR–C and 1Pt–CeR–C. These results clearly demonstrate that Pt single atoms were deposited on catalysts with the CeR–C support but both single atoms and clusters co-existed on 1Pt–Ce–C. This is in good agreement with the HAADF-STEM results (Fig. 1b–e). While both 0.3Pt–CeR–C and 1Pt–CeR–C contained Pt single atoms, X-ray absorption near edge spectroscopy (XANES) results showed that Pt on 0.3Pt–CeR–C was more oxidized than that on 1Pt–CeR–C, as evidenced by higher white line intensity (Fig. S8).
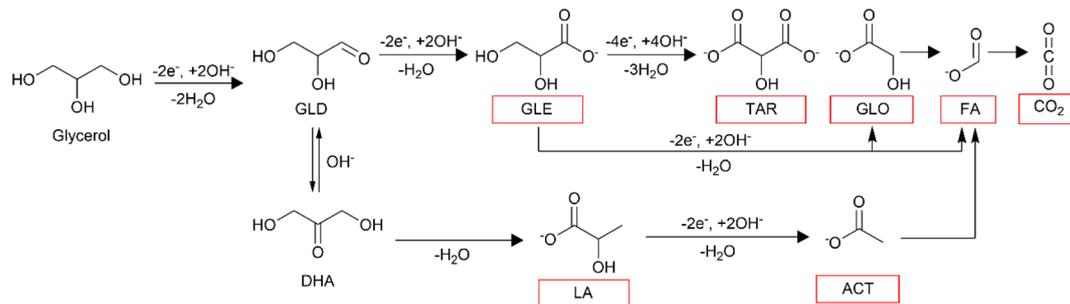
3.2. Electrochemical measurements and GEOR

The electrocatalytic performance of the synthesized catalysts and 20% Pt/C was initially investigated in an aqueous solution of 1 M KOH. CVs of the catalysts were recorded in 1 M KOH with a scan rate of 10 mV s^{-1} and the results are shown in Fig. S9. In 1 M KOH, no distinct hydrogen underpotential deposition

(H_{upd}) peak of Pt was observed for the Pt-ceria-carbon catalysts in the range of 0.05–0.4 V_{RHE}. The H_{upd} peak was not obvious due to the atomic-sized Pt[32] and/or the broad adsorption/desorption peak of ceria in the same range.

The presence of only single atoms on 0.3Pt–CeR–C and 1Pt–CeR–C was further confirmed using the MOR. It is known that the MOR requires at least three consecutive Pt atoms on the surface. Pt ensembles are needed to adsorb methanol and then activate the C–H/C–O bond.[33,34] Isolated Pt atoms are not able to provide these contiguous sites and therefore remain inactive toward the MOR. Hence, the MOR can be used as a probe reaction to verify the existence of Pt clusters.[35,36] In Fig. S10a, 0.3Pt–CeR–C and 1Pt–CeR–C did not show any activity towards the MOR. However, 1Pt–Ce–C, in which Pt clusters were present, exhibited noticeable MOR activity. 1Pt NP-CeR–C and Pt/C, which contained Pt nanoparticles, showed high MOR activity. The CeR–C support itself did not show any MOR activity, indicating that MOR activity was only from Pt clusters or nanoparticles (Fig. S10b). These MOR results prove that Pt in the 0.3Pt–CeR–C and 1Pt–CeR–C was atomically dispersed without Pt cluster formation.

15078 | J. Mater. Chem. A, 2026, **14**, 15075–15084

This journal is © The Royal Society of Chemistry 2026

Scheme 1 GEOR pathways on Pt catalysts. GLD: glyceraldehyde; GLE: glycerate; TAR: tartronate; LA: lactate; GLO: glycolate; ACT: acetate; FA: formate. The products detected in this work are denoted with a red box.

Next, the GEOR was measured by the CA method. In the aqueous solution of 1 M KOH + 0.1 M glycerol, the catalyst-loaded carbon paper was immersed, and the constant potentials of 0.6, 0.8, 1.0, and 1.2 V_{RHE} were applied for 3 h. The CA curves are presented in Fig. S11. The GEOR on Pt catalysts can produce C_3 intermediates of glyceraldehyde (GLD) and dihydroxyacetone (DHA), further oxidized into C_3 products of glycerate (GLE), lactate (LA), and tartronate (TAR) (Scheme 1). Under alkaline conditions, DHA rapidly converts to GLD (e.g., via aldol condensation), making it difficult to be obtained in measurable amounts.[37,38] These C_3 products may be oxidized more into C_2 products of glycolate (GLO) and acetate (ACT), or C_1 products of formate (FA) and CO_2 through C–C bond cleavage.[39]

Fig. S12 shows the productivities obtained after 3 h of electrooxidation at each potential. The specific productivity and selectivity of each product with detailed glycerol conversion and faradaic efficiency are presented in Table S2. The NMR data and GC results are shown in Fig. S13 and S14. For the catalysts composed predominantly of atomically dispersed Pt, GLE was the most dominant product at every potential. In the case of 1Pt-CeR-C, GLE productivity reached 15.4 mmol L^{-1} mg_{Pt}^{-1} h^{-1} at 1.2 V_{RHE}, which was more than twice that at 0.6 V_{RHE}. 0.3Pt-CeR-C and 1Pt-Ce-C also showed a similar trend; the GLE productivity increased as the potential increased. In contrast, for the catalysts with Pt nanoparticles, C_2 and C_1 products were generated more as the potential increased. 1Pt NP-CeR-C and Pt/C showed GLO, containing two carbons, as their dominant product from 1.0 V_{RHE}. The FA productivity increased significantly upon potential increase for Pt/C, from 1.2 mmol L^{-1} mg_{Pt}^{-1} h^{-1} at 0.6 V_{RHE} to 4.9 mmol L^{-1} mg_{Pt}^{-1} h^{-1} at 1.0 V_{RHE}. This comparison indicates that Pt single atoms preserved the C_3 framework better while Pt nanoparticles cleaved the C–C bond generating more C_2 or C_1 products.

The C_3, C_2, and C_1 selectivity for various catalysts is summarized in Fig. 2. In most Pt-based catalysts, the high anodic potential facilitates C–C bond cleavage, leading to further oxidized C_2 and C_1 chemicals.[21,39–41] This trend was clearly observed for the catalysts with Pt nanoparticles. The selectivity for C_3 products decreased from 60.0% to 39.3% for 1Pt NP-CeR-C, and from 73.9% to 34.9% for Pt/C, respectively (Fig. 2c and e). Similarly, the catalysts with Pt clusters (1Pt-Ce-C, 1.5Pt-CeR-C, and 2Pt-CeR-C) also exhibited a potential-

dependent decline in C_3 selectivity (Fig. 2d and S15). This further supports that Pt nanoparticles and clusters promote C–C bond scission at elevated potentials.

However, it was notable that the selectivity for C_3 was nearly maintained in Pt single atoms when the potential increased to 1.2 V_{RHE}, while only slightly decreasing from 83.5% to 77.4% for 0.3Pt-CeR-C, and from 69.7% to 63.6% for 1Pt-CeR-C, respectively. Whereas the C_3 selectivity was the highest in 0.3Pt-CeR-C, the GLE productivity was much higher in 1Pt-CeR-C, probably due to more active sites with metallic features. When only GLE selectivity was counted, the difference between Pt single atoms and Pt nanoparticles seemed more pronounced. A decline in GLE selectivity was observed for Pt/C (from 37.1% to 19.1%), whereas an increase in GLE selectivity was observed for 1Pt-CeR-C (from 43.0% to 51.6%) when the potential increased from 0.6 to 1.2 V_{RHE} (Table S2).

When the sum of all the detectable products was considered, the total productivity increased as the potential increased for 1Pt-CeR-C, 0.3Pt-CeR-C, and 1Pt-Ce-C (Fig. 2f). 1Pt-CeR-C especially showed a large increase in the total productivity from 15.3 mmol L^{-1} mg_{Pt}^{-1} h^{-1} at 0.6 V_{RHE} to 29.1 mmol L^{-1} mg_{Pt}^{-1} h^{-1} at 1.2 V_{RHE}. However, 1Pt NP-CeR-C and Pt/C reached their maximum productivity at 0.8 V_{RHE} and then decreased afterward. In particular, Pt/C presented a significant decrease in the total productivity at 1.2 V_{RHE}, in which the carbon support would be corroded causing Pt detachment.[42] The electrochemical surface area (ECSA) truly decreased from 32.4 to 23.1 m^2 g_{Pt}^{-1} after the GEOR at 1.2 V_{RHE} for 3 h (Fig. S16a). However, there was no change in CV curves for 1Pt-CeR-C after the same reaction (Fig. S16b). The ceria deposited on the carbon support could act as an electron sink benefiting from the redox cycle between Ce^{3+} and Ce^{4+}, preventing carbon oxidation.[43]

The GEOR catalytic properties were further investigated under various electrolyte conditions to evaluate their effect on product selectivity. When the cation effect was evaluated for 1 M KOH, NaOH, and LiOH aqueous solutions (Fig. S17), the GEOR at 1Pt-CeR-C presented little change upon cation change, while Pt/C produced slightly more LA as the cation size decreased. Such cation effects are commonly attributed to differences in the hydration shell that modify interfacial interactions.[44,45] Wu et al. proposed that cations selectively associate with glycerol-oxidation intermediates, thereby altering the final product distribution.[46]
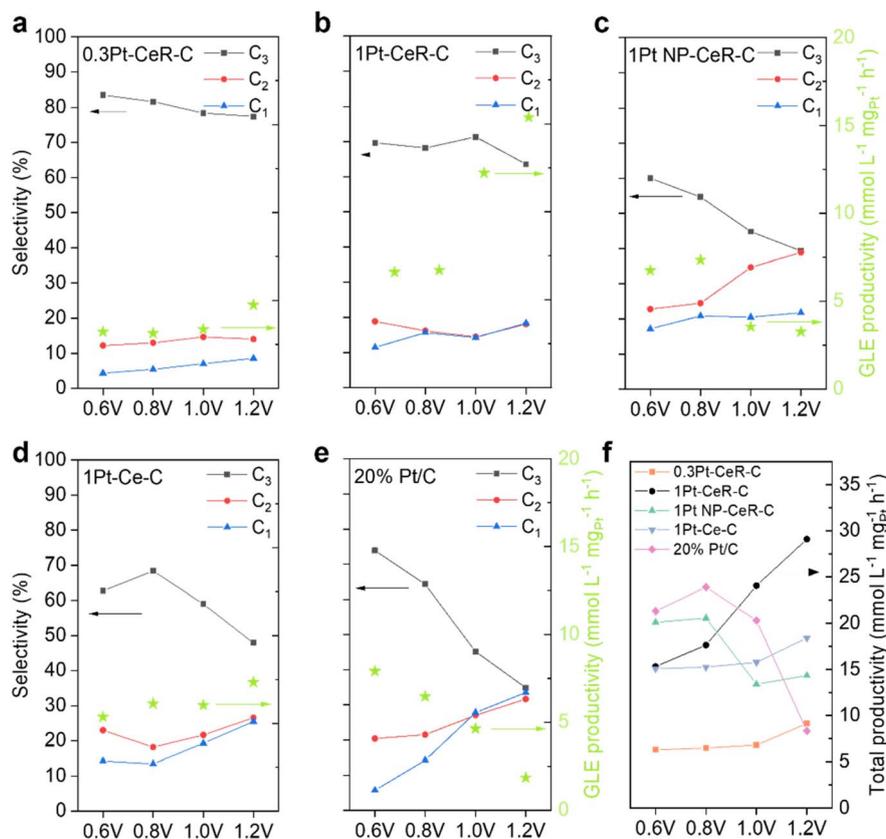
This journal is © The Royal Society of Chemistry 2026

J. Mater. Chem. A, 2026, **14**, 15075–15084 | **15079**

Fig. 2 The selectivity of C_3, C_2, and C_1 at each potential (*vs.* RHE) for (a) 0.3Pt-CeR-C, (b) 1Pt-CeR-C, (c) 1Pt NP-CeR-C, (d) 1Pt-Ce-C, and (e) Pt/C. The right *y*-axis (denoted as a green star) reflects the GLE productivity at each potential. (f) The total productivity at each potential.

The minimal variation observed for 1Pt-CeR-C suggested that isolated Pt sites were relatively insensitive to the cation effect, compared with Pt nanoparticles. When a neutral electrolyte (pH 7) was used instead of an alkaline electrolyte, the total productivity decreased greatly producing TAR.

3.3. *In situ* Raman spectroscopy analysis

In order to examine whether the adsorption of glycerol is affected by the Pt atomic configuration, *in situ* Raman spectroscopy was conducted during the GEOR in 1 M KOH + 0.5 M glycerol at various potentials (Fig. 3a–c and S18). The characteristic C–C stretching vibration modes ($\nu_s(C–C)$) of glycerol were observed at 819 and 851 cm^{-1}.[47] The CH_2 rocking vibrations ($\tau(CH_2)$) were detected at 913 and 975 cm^{-1}. Bands within 1020–1080 cm^{-1} and 1088–1130 cm^{-1} correspond to C–OH stretching ($\nu_s(C–OH)$) from the terminal and central carbons of glycerol, respectively.[48,49] In particular, the sharp peak at 1061 cm^{-1} was observed when using Pt nanoparticles as a working electrode. Li *et al.* suggested that the Raman peak at 1061 cm^{-1} is derived from the glycerol adsorption on the surface *via* bonding with two terminal C atoms of glycerol molecules, as shown in the left scheme of Fig. 3d.[10] The bidentate adsorption of glycerol causes this peak through interaction with 1,3 terminal C atoms and the multiple Pt sites on the Pt nanoparticle. In case of Pt/C, this peak became more distinct with sharpness as the applied potential increased,

indicating that glycerol tended to be adsorbed on the Pt surface in a parallel way. In contrast, the catalysts with Pt single atoms showed only a broad peak in the $\nu_s(C–OH)$ stretching band, and there was little change in Raman peaks although potentials were varied. Even with an increase in potential, adsorptions with two terminal carbons were restricted on the Pt single atom catalyst. The single atomic feature probably allowed the adsorption of only one terminal carbon, as shown in the right scheme of Fig. 3d.

At low potentials, Pt-based catalysts predominantly favor oxidative dehydrogenation, producing GLE as the main product.[21,50] At elevated potentials, C–C bond cleavage becomes more favorable, and conventional Pt catalysts typically produce C_2 or C_1 chemicals, mainly GLO and FA.[51] Anil *et al.* demonstrated that the Pt catalyst follows the pathway towards oxalic acid and formic acid at high potentials.[52] It was reported that the conversion of GLE (C_3 product) to GLO (C_2 product) requires the stabilization of multivalent carbon-binding intermediates on the catalyst surface.[53] Pt single-atom catalysts do not provide contiguous Pt sites capable of binding multiple carbon atoms of one GLE molecule. Therefore, the Pt single-atom configuration substantially inhibited C–C cleavage, resulting in dominant oxidative dehydrogenation of glycerol to GLE and a diminished GLE → GLO → FA pathway even at high potentials.

Some studies suggested that ceria can promote OH adsorption and facilitate OH spillover to Pt active sites.[54,55] To examine
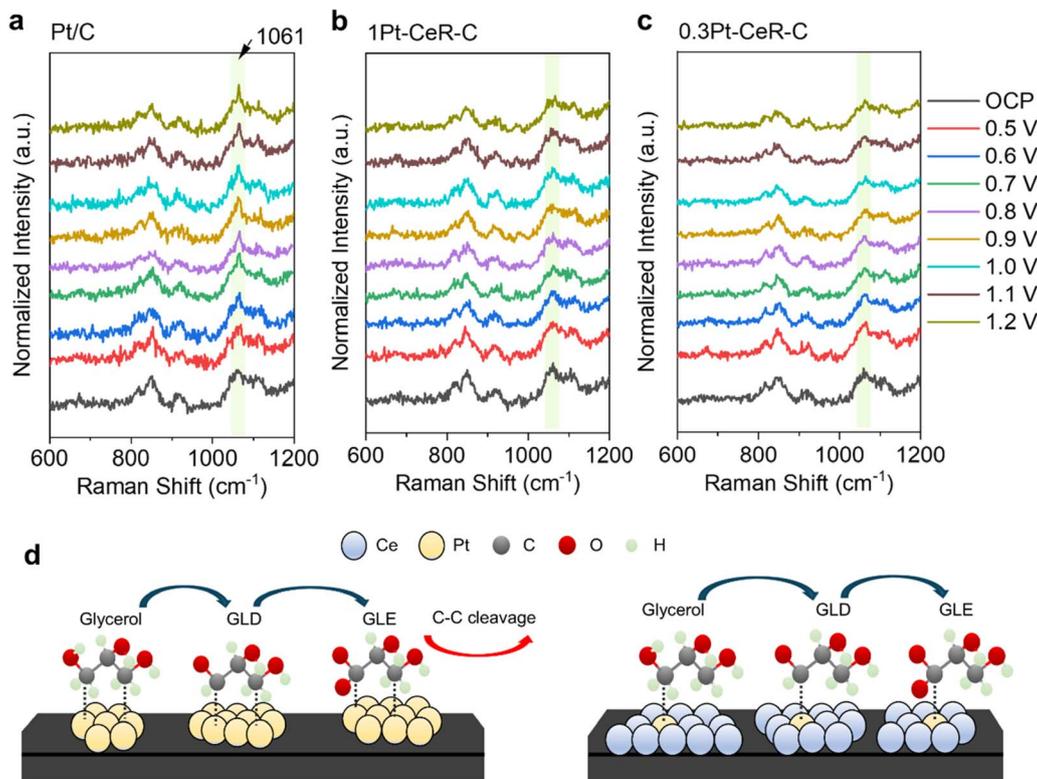
15080 | *J. Mater. Chem. A*, 2026, **14**, 15075–15084

This journal is © The Royal Society of Chemistry 2026

Fig. 3   *In situ* Raman spectra recorded for (a) Pt/C, (b) 1Pt–CeR–C and (c) 0.3Pt–CeR–C at varied potentials in 1 M KOH + 0.5 M glycerol. (d) Schematic diagram of glycerol adsorption on a Pt nanoparticle and a Pt single atom.

whether ceria affected the adsorbates on the catalyst surface, *in situ* Raman spectra near 460 cm^{-1} were compared in 1 M KOH with increasing potential (Fig. S19), where both peaks of Pt–OH$_{(ads)}$ and Ce–OH$_{(ads)}$ appear.[10,56] Regardless of potentials, 1Pt–CeR–C and Pt/C presented similar spectra, making the role of ceria in the surface reaction inconclusive. Compared with the Pt/C, 1Pt–CeR–C did not show significantly enhanced *OH formation. These results imply that the distinct difference in the GEOR activity would result from a different Pt configuration, not from the existence of ceria.

3.4.   Testing catalyst stability and operating in a flow cell

The GEOR was performed at 1.0 V$_{RHE}$ for 48 h to evaluate the catalyst stability of 1Pt–CeR–C and Pt/C (Fig. 4). The initial selectivity, which was observed for the first 3 h, was mostly maintained, reaching GLE productivity of 249 mmol L^{-1} mg$_{Pt}^{-1}$ at 48 h in 1Pt–CeR–C. The 1Pt–CeR–C catalyst was stable enough to sustain its high C$_3$ selectivity by maintaining Pt single atoms without agglomeration. Fig. S20a shows HAADF-STEM images of 1Pt–CeR–C obtained after 48 h of operation, indicating that the Pt single atoms were still clearly observed. Moreover, ceria maintained its structure without aggregation. The crystalline size of ceria estimated from XRD data *via* the Scherrer equation remained at 5.8 nm after the reaction (Fig. S21). In the Pt/C, GLO was produced the most in the early stage, but more FA was formed at 48 h. A shift in the products from C$_3$ to C$_2$ to C$_1$ was observed, indicating the eventual cleavage of the C–C bond

over time. The Pt nanoparticles were greatly aggregated after reaction for 48 h (Fig. S20b).

Beyond batch operation, flow cell configurations are regarded as an industrially relevant operation because they couple high-rate chemistry with continuous processing.[57] The flow cells can enhance mass activity and faradaic efficiency by reducing diffusion-layer thickness and mitigating ohmic losses.[58] Moreover, continuous flow enables immediate downstream separation and integration with inline separation technologies.[59] Hence, to better approximate industrial operation, the GEOR of 1Pt–CeR–C at various potentials was tested further using a flow cell, whose scheme and photograph are shown in Fig. 5a. Even using the flow cell, 1Pt–CeR–C maintained its high C$_3$ selectivity and high GLE selectivity (50.6%) even at the potential of 1.2 V$_{RHE}$ (Fig. 5b). Moreover, the flow cell assisted to achieve higher GLE productivities than the batch reactor, due to minimized charge transfer resistance. The distance between the anode and cathode was significantly reduced to ~5 mm in the flow cell. The GLE productivity reached up to 21.7 mmol L^{-1} mg$_{Pt}^{-1}$ h^{-1} at 1.2 V$_{RHE}$. The *i–t* curves recorded using the flow cell are shown in Fig. S22. The specific productivity and selectivity of each product with detailed glycerol conversion and faradaic efficiency are presented in Table S3.

Additionally, to evaluate and optimize the key flow-cell parameters, control experiments were conducted by varying the electrolyte flow rate and glycerol concentration (Fig. S23 and Table S4). The potential of 1.2 V$_{RHE}$ was applied for 3 h to
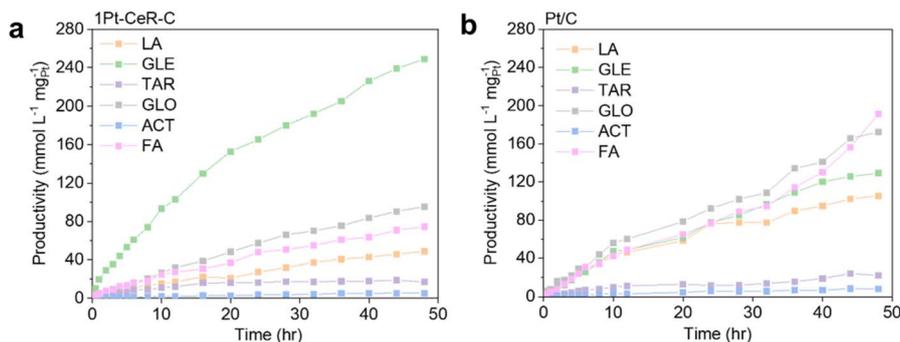
Fig. 4 The changes in the GEOR products as a function of time for (a) 1Pt-CeR-C and (b) Pt/C at an applied potential of 1.0 V_{RHE} for 48 h in 1 M KOH + 0.1 M glycerol.

maximize the productivity. Increasing the flow rate from 10 sccm to 20 sccm led to a negligible change in productivity. In contrast, increasing the glycerol concentration from 0.1 M to 0.5 M resulted in a significant increase in GLE productivity, reaching 37.0 mmol L^{-1} mg_{Pt}^{-1} h^{-1}, with a GLE selectivity of 51.6% at 1.2 V_{RHE}. The GLE productivity was compared with the literature values in Table S5, showing that our value of maximum GLE productivity is even higher than the best values reported so far.

To address the feasibility of industrial application, long-term stability was evaluated using an enlarged 5 cm² flow cell. A

chronoamperometric test was conducted at 1.0 V_{RHE} for 100 h (Fig. 5c). 1Pt-CeR-C maintained stable current throughout 100 h of operation, indicating sustained electrochemical activity under prolonged applied potential. Importantly, the catalyst exhibited continuous product formation throughout the 100 h operation, suggesting that catalyst degradation and poisoning barely occurred during the stability test. High cumulative GLE productivity was achieved with 3290 mmol L^{-1} mg_{Pt}^{-1} at 100 h. The high C_3 selectivity was also maintained, indicating that C–C cleavage was suppressed during the extended operation (Table S6).
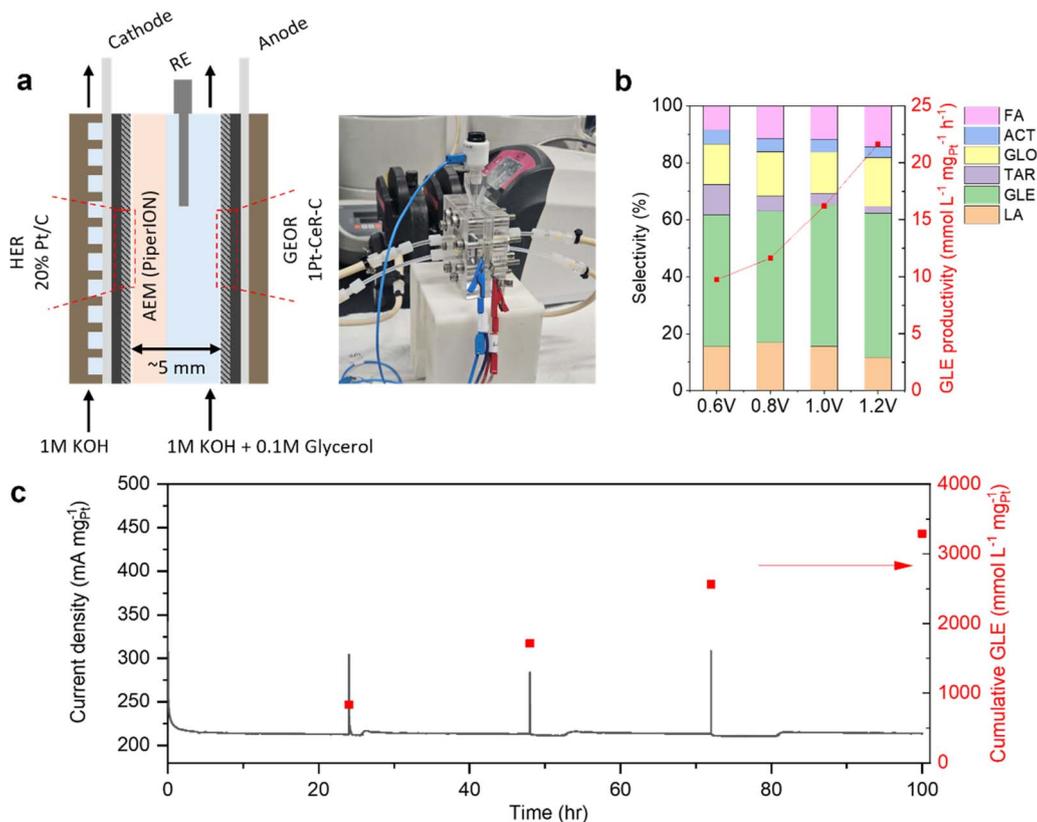

Fig. 5 (a) A scheme and a photograph of the flow cell. (b) The selectivity and GLE productivity for the GEOR of 1Pt-CeR-C for 3 h using the 1 cm² flow cell in 1 M KOH + 0.1 M glycerol. (c) I–t curve with cumulative GLE productivity of 1Pt-CeR-C for a 100 h stability test using the 5 cm² flow cell at 1.0 V_{RHE} in 1 M KOH + 0.5 M glycerol. Electrolytes were refreshed every 24 h.

15082 | J. Mater. Chem. A, 2026, 14, 15075–15084

This journal is © The Royal Society of Chemistry 2026

4. Conclusions

This work demonstrates that the structural nature of Pt – whether atomically dispersed or in nanoparticles – dictates the selectivity of glycerol electrooxidation in alkaline media. Pt single atoms were stabilized on defect-rich ceria, which was immobilized on carbon supports. This catalyst exhibited high C_3 selectivity, nearly 70% at various potentials, in glycerol electrooxidation and sustained selective GLE formation even at a high potential of 1.2 V_{RHE}. However, Pt nanoparticles on the same support and Pt/C underwent extensive C–C cleavage and C_3 product selectivity decreased as potential increased, forming more C_2 or C_1 products (GLO and FA). In situ Raman spectroscopy results showed that unlike the Pt nanoparticles, the Pt single-atom catalyst did not have a distinct multi-carbon adsorption state, which could suppress C–C bond cleavage. The single atomic feature was stable for long-term GEOR, while Pt nanoparticles in Pt/C were aggregated. The Pt single atom catalyst was further applied in a flow cell, producing outstanding GLE productivity (37.0 mmol L^{-1} mg_{Pt}^{-1} h^{-1}) with a GLE selectivity of 51.6% at 1.2 V_{RHE}. These findings underline the important role of atomic dispersion of the Pt catalyst in controlling reaction pathways and selectivity for the GEOR.

Author contributions

H. L. proposed, designed and supervised the project. H. R. L synthesized the catalysts, performed characterization, carried out electrochemical analysis, and wrote the manuscript. E. L. and Y. J. H. carried out in situ Raman spectroscopy. Y. C. carried out STEM of the catalysts. J. K., S. J., and S. P. helped with characterization and analysed the data.

Conflicts of interest

There are no conflicts to declare.

Data availability

The data supporting this article have been included as part of the supplementary information (SI). Supplementary information: Fig. S1–S23, Tables S1–S6. See DOI: https://doi.org/10.1039/d6ta00127k.

Acknowledgements

Notes and references

1 IEA, Renewables 2023 Aanalysis and Forecast to 2028, Paris, 2024.

2 D. Singh, D. Sharma, S. L. Soni, S. Sharma, P. Kumar Sharma and A. Jhalani, Fuel, 2020, 262, 116553.

3 M. R. Monteiro, C. L. Kugelmeier, R. S. Pinheiro, M. O. Batalha and A. da Silva César, Renew. Sustain. Energy Rev., 2018, 88, 109–122.

4 Z. Pirzadi and F. Meshkani, Fuel, 2022, 329, 125044.

5 H. Wang, H. Li, C. K. Lee, N. S. Mat Nanyan and G. S. Tay, Int. J. Biol. Macromol., 2024, 261, 129536.

6 A. L. Olson, M. Tunér and S. Verhelst, Heliyon, 2023, 9, e13041.

7 C. A. G. Quispe, C. J. R. Coronado and J. A. Carvalho Jr, Renew. Sustain. Energy Rev., 2013, 27, 475–493.

8 J. J. Bozell and G. R. Petersen, Green Chem., 2010, 12, 539–554.

9 Y. He, Z. Ma, F. Yan, C. Zhu, T. Shen, S. Chou, X. Zhang and Y. Chen, Proc. Natl. Acad. Sci. U. S. A., 2024, 121, e2320777121.

10 Y. Li, X. Wei, R. Pan, Y. Wang, J. Luo, L. Li, L. Chen and J. Shi, Energy Environ. Sci., 2024, 17, 4205–4215.

11 Y. Li, X. Wei, L. Chen, J. Shi and M. He, Nat. Commun., 2019, 10, 5335.

12 Y. Zhou, Y. Shen and J. Piao, ChemElectroChem, 2018, 5, 1636–1643.

13 E. Skrzyńska, A. Wondołowska-Grabowska, M. Capron and F. Dumeignil, Appl. Catal., A, 2014, 482, 245–257.

14 S. A. N. M. Rahim, C. S. Lee, F. Abnisa, M. K. Aroua, W. A. W. Daud, P. Cognet and Y. Pérès, Sci. Total Environ., 2020, 705, 135137.

15 M. K. Goetz, E. Usman and K.-S. Choi, ACS Catal., 2023, 13, 15758–15769.

16 M. Yoo, D. Choi, M. Shin, S. Jung, J. Lee and H. J. Kim, Chem. Eng. J., 2025, 518, 164743.

17 L. Xu, Y. Yang, C. Li, R. Ning, J. Ma, M. Yao, S. Geng and F. Liu, Chem. Eng. J., 2024, 481, 148304.

18 N. Kondamudi, M. Misra, S. Banerjee, S. Mohapatra and S. Mohapatra, Appl. Catal., B, 2012, 126, 180–185.

19 A. Corma, S. Iborra and A. Velty, Chem. Rev., 2007, 107, 2411–2502.

20 Y. Kwon, K. J. P. Schouten and M. T. M. Koper, ChemCatChem, 2011, 3, 1176–1185.

21 I. Terekhina and M. Johnsson, Nanoscale, 2024, 16, 13000–13010.

22 A. C. Garcia, M. J. Kolb, C. van Nierop y Sanchez, J. Vos, Y. Y. Birdja, Y. Kwon, G. Tremiliosi-Filho and M. T. M. Koper, ACS Catal., 2016, 6, 4491–4500.

23 C. Dai, L. Sun, H. Liao, B. Khezri, R. D. Webster, A. C. Fisher and Z. J. Xu, J. Catal., 2017, 356, 14–21.

24 T. Li and D. A. Harrington, ChemSusChem, 2021, 14, 1472–1495.

25 S. Shin, H.-E. Kim, B.-S. Kim, S. S. Jeon, H. Jeong and H. Lee, ChemElectroChem, 2020, 7, 3716–3719.

26 S. Xie, S. Liu, Y. Lu, C. Wang, S. Cao, W. Diao, J. Deng, W. Tan, L. Ma, S. N. Ehrlich, Y. Li, Y. Zhang, K. Ye, H. Xin, M. Flytzani-Stephanopoulos and F. Liu, J. Am. Chem. Soc., 2022, 144, 21255–21266.

27 C. Ding, Q. Gu, L.-J. Yu, S. Zhang, Y. Zhang, Z. Ma, Y. Meng, H. Zhang, T. Wang, J. Wang, L. Ma, G. Li, B. Yang and T. Zhang, J. Am. Chem. Soc., 2023, 145, 2523–2531.

This journal is © The Royal Society of Chemistry 2026

J. Mater. Chem. A, 2026, 14, 15075–15084 | 15083

28 H. Jeong, O. Kwon, B.-S. Kim, J. Bae, S. Shin, H.-E. Kim, J. Kim and H. Lee, *Nat. Catal.*, 2020, **3**, 368–375.

29 L. Zhang, G. Spezzati, V. Muravev, M. A. Verheijen, B. Zijlstra, I. A. W. Filot, Y.-Q. Su, M.-W. Chang and E. J. M. Hensen, *ACS Catal.*, 2021, **11**, 5614–5627.

30 V. Giulimondi, M. Vanni, S. Damir, T. Zou, S. Mitchell, F. Krumeich, A. Ruiz-Ferrando, N. López, J. J. Gata-Cuesta, G. Guillén-Gosálbez, J. J. Smit, P. Johnston and J. Pérez-Ramírez, *ACS Catal.*, 2024, **14**, 13652–13664.

31 J. H. Kim, D. Shin, J. Lee, D. S. Baek, T. J. Shin, Y.-T. Kim, H. Y. Jeong, J. H. Kwak, H. Kim and S. H. Joo, *ACS Nano*, 2020, **14**, 1990–2001.

32 J.-F. Huang, W.-J. Hsieh and J.-L. Chen, *ACS Appl. Mater. Interfaces*, 2024, **16**, 27504–27510.

33 N.-D. Tran, M. Farnesi Camellone and S. Fabris, *J. Phys. Chem. C*, 2018, **122**, 17917–17927.

34 A. Cuesta, *J. Am. Chem. Soc.*, 2006, **128**, 13332–13333.

35 J. Kim, H.-E. Kim and H. Lee, *ChemSusChem*, 2018, **11**, 104–113.

36 H.-E. Kim, I. H. Lee, J. Cho, S. Shin, H. C. Ham, J. Y. Kim and H. Lee, *ChemElectroChem*, 2019, **6**, 4757–4764.

37 C. Zhou, J. Chen, J. Zhao, Y. Meng, Z. Li, X. Meng and J. Wang, *Renewables*, 2024, **2**, 89–110.

38 H. Ye, S. Favero, H. Tyrrell, K. Plub-in, A. Hankin, R. R. Rao, I. E. L. Stephens, M.-M. Titirici and H. Luo, *ChemCatChem*, 2025, **17**, e00152.

39 I. Terekhina, J. White, A. Cornell and M. Johnsson, *ACS Appl. Nano Mater.*, 2023, **6**, 11211–11220.

40 T. Chen, C. Guan, F. Yao, X. Qi, J. Yu, J. Du, L. Lv, H. Wei and H. Chu, *J. Rare Earths*, 2025, **43**, 453–461.

41 J. White, I. Terekhina, E. Campos dos Santos, D. Martín-Yerga, L. G. M. Pettersson, M. Johnsson and A. Cornell, *ACS Appl. Energy Mater.*, 2024, **7**, 1802–1813.

42 K. Zhao, S. Han, L. Ke, X. Wu, X. Yan, X. Cao, L. Li, X. Jiang, Z. Wang, H. Liu and N. Yan, *ACS Catal.*, 2023, **13**, 2813–2821.

43 Z.-K. Han, W. Liu and Y. Gao, *JACS Au*, 2025, **5**, 1549–1569.

44 S. Ringe, E. L. Clark, J. Resasco, A. Walton, B. Seger, A. T. Bell and K. Chan, *Energy Environ. Sci.*, 2019, **12**, 3001–3014.

45 J. Noh, H. Kim, H. Park and D. Y. Chung, *ACS Catal.*, 2025, **15**, 7780–7791.

46 J. Wu, J. Li, Y. Li, X.-Y. Ma, W.-Y. Zhang, Y. Hao, W.-B. Cai, Z.-P. Liu and M. Gong, *Angew. Chem., Int. Ed.*, 2022, **61**, e202113362.

47 E. Mendelovici, R. L. Frost and T. Kloprogge, *J. Raman Spectrosc.*, 2000, **31**, 1121–1126.

48 C. Liu, M. Hirohara, T. Maekawa, R. Chang, T. Hayashi and C.-Y. Chiang, *Appl. Catal., B*, 2020, **265**, 118543.

49 J. Zhang, Y. Shen and H. Li, *ACS Appl. Energy Mater.*, 2023, **6**, 5508–5518.

50 I. Terekhina and M. Johnsson, *ACS Appl. Mater. Interfaces*, 2024, **16**, 56987–56996.

51 Y. Liu, W. Yu, D. Raciti, D. H. Gracias and C. Wang, *J. Phys. Chem. C*, 2019, **123**, 426–432.

52 A. Anil, J. White, E. Campos dos Santos, I. Terekhina, M. Johnsson, L. G. M. Pettersson, A. Cornell and G. Salazar-Alvarez, *J. Mater. Chem. A*, 2023, **11**, 16570–16577.

53 N. Lyu, Y. Chen, A. Guan, R. Wei, C. Yang, Y. Huang, X. Lv, C. Hu, M. Kuang and G. Zheng, *Small*, 2024, **20**, 2401872.

54 J. Li, Z. Li, Z. Zheng, X. Zhang, H. Zhang, H. Wei and H. Chu, *ChemCatChem*, 2022, **14**, e202200509.

55 F. S. Cursi, L. Grimaud, J. Rousseau, K. Servat, C. Morais, T. W. Napporn, A. R. de Andrade and K. B. Kokoh, *ChemElectroChem*, 2024, **11**, e202300555.

56 K. K. Patra, Z. Liu, H. Lee, S. Hong, H. Song, H. G. Abbas, Y. Kwon, S. Ringe and J. Oh, *ACS Catal.*, 2022, **12**, 10973–10983.

57 A. A. Folgueiras-Amador and T. Wirth, *J. Flow Chem.*, 2017, **7**, 94–95.

58 T. P. Nicholls, C. Schotten and C. E. Willans, *Curr. Opin. Green Sustainable Chem.*, 2020, **26**, 100355.

59 T. Noël, Y. Cao and G. Laudadio, *Acc. Chem. Res.*, 2019, **52**, 2858–2869.

15084 | *J. Mater. Chem. A*, 2026, **14**, 15075–15084

This journal is © The Royal Society of Chemistry 2026